ADVANCED FUNCTIONAL MATERIALS
www.afm-journal.de

Fast and Large Lithium Storage in 3D Porous VN Nanowires–Graphene Composite as a Superior Anode Toward High-Performance Hybrid Supercapacitors

*Rutao Wang, Junwei Lang, Peng Zhang, Zongyuan Lin, and Xingbin Yan**

Li-ion hybrid capacitors (LIHCs), consisting of an energy-type redox anode and a power-type double-layer cathode, are attracting significant attention due to the good combination with the advantages of conventional Li-ion batteries and supercapacitors. However, most anodes are battery-like materials with the sluggish kinetics of Li-ion storage, which seriously restrict the energy storage of LIHCs at the high charge/discharge rates. Herein, vanadium nitride (VN) nanowire is demonstated to have obvious pseudocapacitive characteristic of Li-ion storage and can get further gains in energy storage through a 3D porous architecture with the assistance of conductive reduced graphene oxide (RGO). The as-prepared 3D VN–RGO composite exhibits the large Li-ion storage capacity and fast charge/discharge rate within a wide working widow from 0.01–3 V (vs Li/Li^+), which could potentially boost the operating potential and the energy and power densities of LIHCs. By employing such 3D VN–RGO composite and porous carbon nanorods with a high surface area of 3343 $m^2 g^{-1}$ as the anode and cathode, respectively, a novel LIHCs is fabricated with an ultrahigh energy density of 162 Wh kg^{-1} at 200 W kg^{-1}, which also remains 64 Wh kg^{-1} even at a high power density of 10 kW kg^{-1}.

1. Introduction

With the surge of market in portable electronic devices and electric vehicles, energy-storage techniques are required to provide high energy and power densities as well as long cycle life.[1,2] In this context, numerous studies have been devoted to improving the performance of energy storage devices, particularly to lithium-ion batteries (LIBs) and supercapacitors (SCs).[3–6] The LIBs commonly can deliver the high energy density (150–200 Wh kg^{-1}), but are limited by their low power density (less than 1000 W kg^{-1}) and poor cycling lifetime (below 1000 cycles) because they operate using the redox reactions that involve the sluggish Li-ion diffusion throughout the active materials.[1,7] In contrast, SCs can deliver much high power density (5–10 kW kg^{-1}) and possess long cycle stability (exceeding 1×10^5 cycles) due to the fast physical adsorption/desorption of solvated ions at the electrolyte–electrode interface, but suffer from much lower energy density (below 10 Wh kg^{-1}).[8] Accordingly, new energy devices are strongly desired to have the combining characteristics in high energy and power densities and long cycle life as a solution to bridge the gap between the LIBs and SCs.

Hybrid Li-ion capacitors (HLICs), as a new type of hybrid energy storage devices, have been proposed to possess the advanced characteristics of both LIBs and SCs.[2,9] Such novel hybrid systems, which combine a porous carbon cathode and a lithium-ion battery-like anode in organic electrolytes containing Li salts, are expected to achieve improvements both in energy and power densities due to the fast charging rate of cathode, the large specific capacity of the anode, and the much wider working voltage window of the organic electrolytes.[2,9–13] However, for most reported HLICs, a high energy density is only obtained at the low charge/discharge current density, and the energy density decreases significantly at the high charge/discharge rate. This can be attributed to the mismatch between the kinetics of two electrodes, where the kinetics of anode based on the faradaic lithium inter/detercalation reaction is far less than that of cathodes using the physical adsorption/desorption of solvated ions at the electrolyte–electrode interface.[14–16] An alternative approach is to use pseudocapacitive anode in which, the kinetics is not diffusion-limited and instead is limited by surface processes, and thus is fast. For example, Nb_2O_5, as a typical pseudocapacitive material, can deliver high storage capacity of ≈100 mA g^{-1} at rate as high as 100 C (≈140 mA g^{-1} at 1 C) in Li-ions related organic electrolytes.[17] Lee et al. further designed the HLICs using Nb_2O_5 anode, which have the high-rate characteristic (an energy density of 15 Wh kg^{-1} is obtained at an extremely large power density of 18.5 kW kg^{-1}).[14] Beside the Nb_2O_5, other electrode materials such as V_2O_5,[18] MoO_3,[19,20] HTi_6O_{13},[21] and TiO_2[22,23] can also provide intercalation or surface redox pseudocapacitances; however, these pseudocapacitive materials are poor electronic conductors and have

Dr. R. Wang, Dr. J. Lang, Dr. P. Zhang, Z. Lin, Prof. X. Yan
Laboratory of Clean Energy Chemistry and Materials
Lanzhou Institute of Chemical Physics
Chinese of Academy of Sciences
Lanzhou 730000, P. R. China
E-mail: xbyan@licp.cas.cn
Dr. J. Lang, Prof. X. Yan
State Key Laboratory of Solid Lubrication
Lanzhou Institute of Chemical Physics
Chinese Academy of Sciences
Lanzhou 730000, P. R. China

DOI: 10.1002/adfm.201404472

the relatively high redox potential (>1.5 V versus Li/Li^+), thus the corresponding HLICs could be only operated below 3.2 V, resulting in a limited energy density. Therefore, it is vital to explore novel pseudocapacitive cathode materials with the low working voltage widow to narrow the kinetics gap between two electrodes and to fully utilize the voltage window of the electrolyte toward the high energy and power density of HLICs.

Vanadium nitride (VN) is a promising negative material candidate for LIBs and SCs because of its good electrical conductivity (≈10^6 Ω^{-1} m^{-1}), wide lithiation potential (0.01–3 V), and high theoretical specific capacity (≈1043 mAh g^{-1}).[24–29] In this work, we reported that, for the first time, VN with the structure of porous nanowires has obvious capacitive charge-storage properties within the wide operating window (0.01–3 V). However, pure VN nanowires only show a specific capacity of 400 mAh g^{-1} at 0.1 A g^{-1} and need further gain in charge storage for the fabrication of hybrid devices. Fortunately, its charge-storage limitation can be effectively solved by creating a 3D porous architecture that combines VN nanowires with graphene. The 3D structure leads to the formation of interconnected pore channels, thus ensuring facile-ion transport and providing access of the electrolyte to the electrode active material. In addition, the highly conductive graphene network further increase the electrical conductivity compared with pure VN nanowires, while the nanowire structure of VN reduces ion diffusion paths. As a result, an improvement in specific capacity (640 mAh g^{-1} at 0.1 A g^{-1}) with a fast pseudocapacitive charge storage process occurs, which benefits greatly to improve both energy and power densities for HLICs. Meanwhile, an activated polyaniline-derived carbon (APDC) with the high BET surface area (3353 m^2 g^{-1}) and good conductivity is used as a positive electrode material to enhance energy storage of hybrid devices. Thereby, by employing these high-performance electrode materials, 3D VN–RGO//APDC HLIC is fabricated with an ultrahigh energy density of 162 Wh kg^{-1} (power density of 200 W kg^{-1}), which also delivers 64 Wh kg^{-1} even at a large power density of 10 kW kg^{-1}.

2. Results and Discussion

The 3D structural VN–RGO composite was prepared by a simple in situ hydrothermal method using graphene and NH_4VO_3 as the precursor, and followed by the annealing process in NH_3 atmosphere (**Figure 1**). The VN–RGO composites with different ratios of graphene and VN were synthesized. The optimal product with ≈19 wt% of graphene (determined by the element analyzer-Vario EL and electrochemical analysis, Figures S1,S2, Supporting Information) was selected and discussed below. **Figure 2**a shows the x-ray diffraction (XRD) profile of as-prepared 3D VN–RGO with pure VN nanowires as contrast, which indicates that the major peaks of the 3D VN–RGO composite can be assign to cubic VN (PDF file 73–0528). The crystallite sizes of VN and 3D VN–RGO calculated using the Scherrer equation, are 13.0 and 12.1 nm, respectively, which indicate that the crystallite size is not obviously changed with the addition of RGO. Furthermore, a wide peak around 26°, corresponding to graphene stacking, are observed in 3D VN–RGO sample. Raman spectra of 3D VN–RGO composite exhibits typical peaks of VO_x oxides coated on VN, and characteristic peaks of graphene (with the G-band and D-band at around 1355 and 1597 cm^{-1}, respectively), which is distinguished with pure VN with only peaks of external VO_x oxides (Figure 2b).[26,29]

The as-prepared VN–RGO with architectures, composed of numerous porous VN nanowires and RGO sheets with 3D interpenetrating network, were observed by scanning electron microscopy (SEM) and transmission electron microscope (TEM) (**Figure 3**, Figures S3,S4, Supporting Information). The lateral sizes of these nanowires are typically in the ranges of 50–100 nm in width and several micrometers in length (Figure 3a,b). A typical HRTEM image (Figure 3c) discloses the lattice fringes with a spacing of 0.236 nm, in good agreement with spacing of (111) plane of VN. Furthermore, the selected area electron diffraction (SAED) patterns of the VN and VN–RGO are shown in Figures 3d and S3c (inset, Supporting Information) which indicate that the VN nanowires is polycrystalline. The elemental

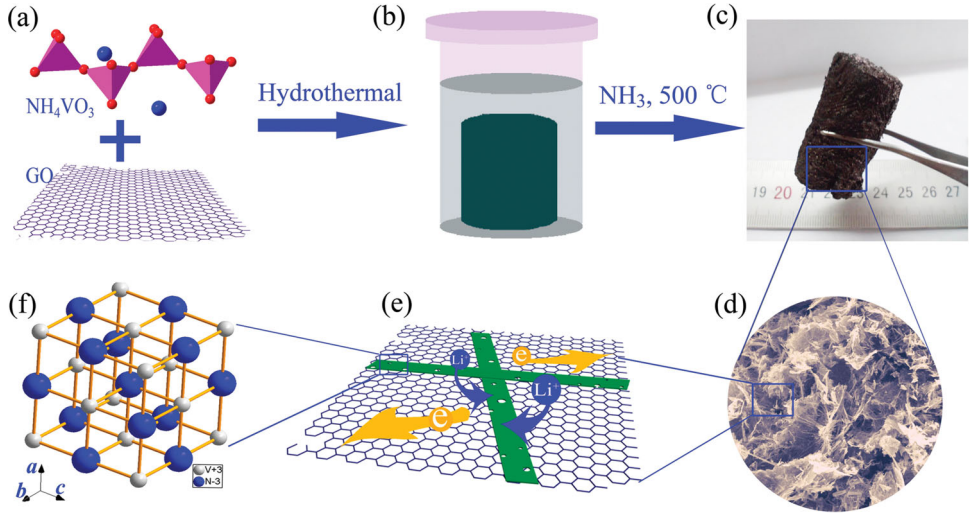

Figure 1. a,b) Schematic of preparing 3D porous VN–RGO composite by a hydrothermal process, and followed by the annealing process in NH_3 atmosphere. c) Optical image of 3D VN–RGO composite. d) SEM image of 3D porous VN–RGO composite. e) Schematic of intimate contacts between the VN nanowires and graphene facilitating charge transport and Li intercalation, f) VN cubic structure.

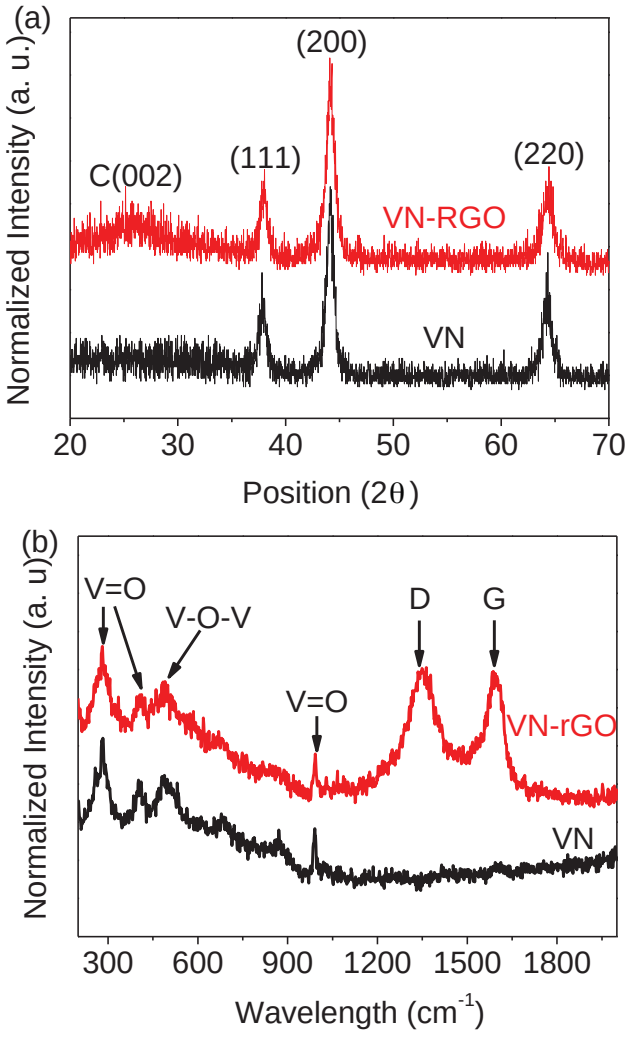

Figure 2. a) XRD patterns; and b) Raman spectra of VN nanowires and 3D VN–RGO composite.

mappings of vanadium, oxygen, nitrogen, and carbon further reveal that the hybrid structure of 3D VN–RGO composite. Moreover, the nitrogen adsorption-desorption isotherm measurements suggest that pure VN nanowires and 3D VN–RGO composite exhibit the hierarchically porous structure composed of abundant smaller mesopores (2–4 nm) and larger meso/macro pores (10–100 nm). It should be noted that with the introduction of graphene, the specific Brunauer–Emmet–Teller (BET) surface area of 3D VN–RGO composite increases by 35.6% from 31.7 to 43 $m^2\ g^{-1}$ as compared with pure VN nanowires (Figure S5, Supporting Information). The increased BET surface area can enhance electrode/electrolyte interface and is beneficial for electrolyte access. In addition, the 3D VN–RGO composite exhibits an electrical conductivity of ≈16.96 S cm^{-1}, which is higher than that of pure VN nanowires (0.85 S cm^{-1}). In short, the above physical-chemical characterization indicates that VN–RGO composite has a highly conductive, 3D porous structure with the high surface area and hierarchical porosity, which is the favorable feature for an enhancement of the electrochemical performance in aspect of the high capacity and fast electrode kinetics.

To investigate the electrochemical performance of pure VN nanowires and 3D VN–RGO composite electrodes, half-cells were prepared using a 2032-type coin cell with lithium metal as the counter and reference electrodes. Cyclic voltammetry (CV) experiments carried out at various scan rates from 0.1 to 100 mV s^{-1} were used to explore the redox processes occurring in the as-prepared VN and VN–RGO electrodes (Figures S6,S7, Supporting Information). As shown in **Figure 4**a, the widely cathodic and anodic current response of VN and VN–RGO is observed between 0.01 and 3 V versus Li/Li^+, which can be attributed to[24,25]

$$VN + xLi^+ + xe^- \leftrightarrow Li_xVN$$

where the maximum capacity is $x = 3$. Generally, the current (i) and scan rates (v) obeys the power law[17,23]

$$i = av^b \quad (1)$$

where a and b are appropriate values. The previous studies show that a b-value of 0.5 indicates a diffusion-controlled process caused by Li intercalation and a b-value of 1 represents a capacitive behavior via a surface faradaic redox reaction.[17,23] Figures 4b and S8 (Supporting Information) presents a plot of log(i) versus log(v) from 0.1 to 100 mV s^{-1} for both cathodic and anodic peaks. For scan rates ranging from 0.1 to 10 mV s^{-1}, the b-value for both the cathode and anodic peaks is greater than 0.85, indicating that the kinetics of VN and VN–RGO is majorly surface-controlled, and thus fast. Figure 4b also shows a change in the slope of the cathodic peaks currents at ≈10 mV s^{-1}. This change in slope corresponds to a decrease in b-value to 0.69–0.76 for the cathodic and anodic currents, respectively, at the sweep rates of 10–100 mV s^{-1}. The limitation in the rate capability at the high scan rates is caused by numerous sources including a diffusion limitations or an increase of the Ohmic contribution.[17] In contrast, pure VN nanowires electrode shows a similar CV feature with 3D VN–RGO composite and a high b-value, suggesting the nature of VN nanowires with fast kinetics. It should be noted that b-value of VN–RGO is slightly higher than that of VN, which indicates that better kinetics can be obtained with the addition of RGO.

To further quantify capacitive contribution to the current response, a novel approach developed by Dunn et al. is used.[30] Accordingly, the current response at a fixed potential can be expressed as being the combination of two separate mechanisms from the concepts discussed above, namely pseudocapacitive effects (k_1v) and diffusion-controlled Li^+ insertion ($k_2v^{1/2}$):[30]

$$i(V) = k_1 v + k_2 \cdot v^{1/2} \quad (2)$$

For further analysis, Equation (2) changes slightly to

$$i(V)/v^{1/2} = k_1 \cdot v^{1/2} + k_2 \quad (3)$$

Using Equation (3), we can determine k_1 and k_2 values at the different potential (V) easily. Figure 4c shows the voltage profile at the scan rate of 0.5 mV s^{-1} for the capacitive currents (shaded area) of VN–RGO as compared with the total

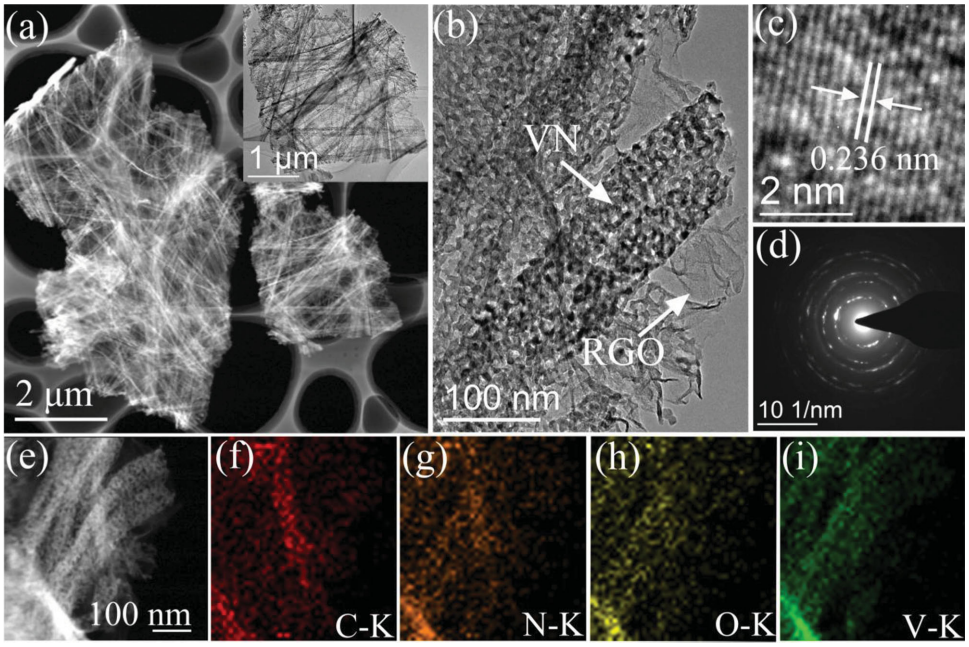

Figure 3. a) Annual dark-field TEM (ADF-TEM) image of 3D VN–RGO composite, inset image is the corresponding bright-field TEM image. b) TEM image of 3D VN–RGO composite. c) High-resolution TEM (HRTEM) image of VN–RGO composite. d) Selected area electron diffraction (SAED) patterns of VN–RGO composite. e) ADF-TEM image of 3D VN–RGO composite and the corresponding element mappings: f) C), g) N, h) O, and i) V.

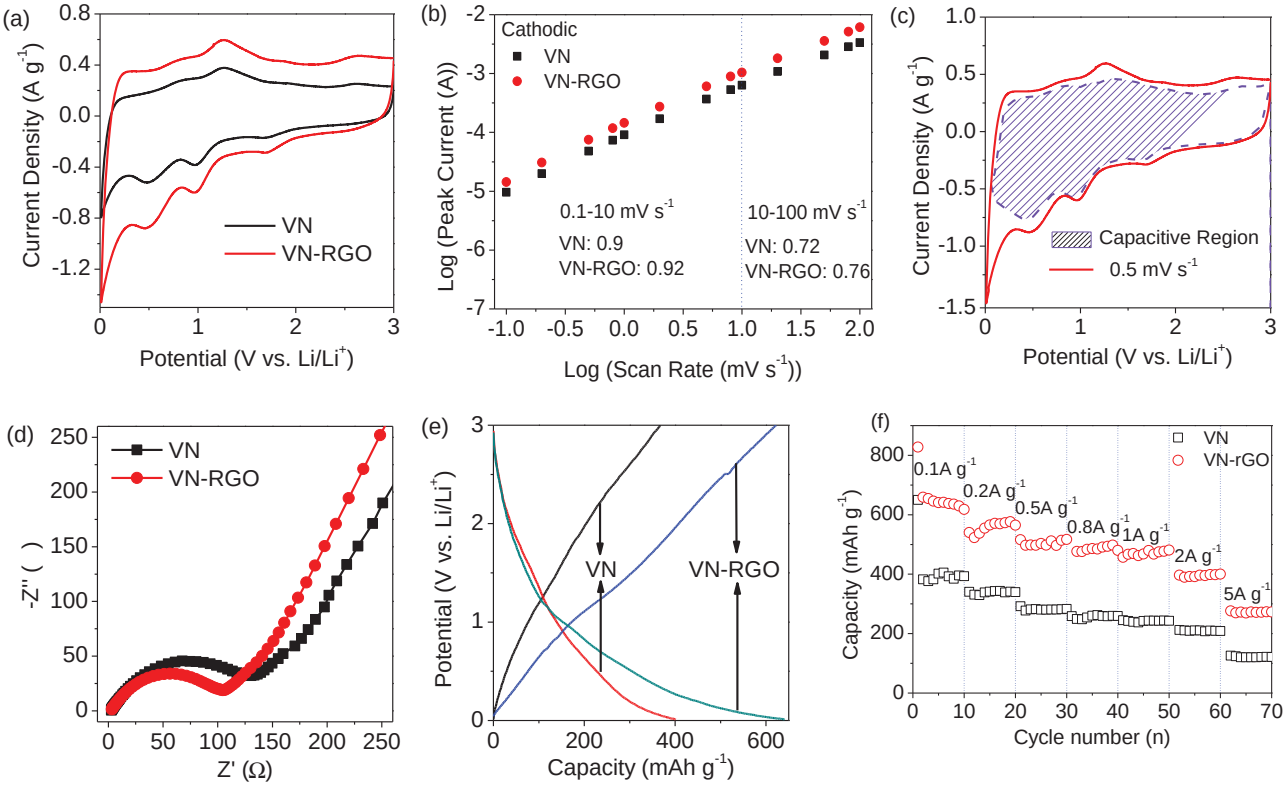

Figure 4. a) CV curves of VN nanowires and 3D VN–RGO composite electrodes at a potential scan rate of 0.5 mV s^{-1}. These curves are recorded after several cycles in order to obtain stable capacities. b) *b*-value determination of the peak cathodic currents shows that charge storage of VN nanowires and 3D VN–RGO composite is capacitive. c) Voltammetric response for 3D VN–RGO electrode at a sweep rate of 0.5 mV s^{-1}. The capacitive contribution to the total current is shown by the shaded region. d) Nyquist plots of VN nanowires and 3D VN–RGO composite electrodes obtained at 1.5 V (vs Li/Li^+). e) The typical charging/discharging curves of VN nanowires and 3D VN–RGO composite electrodes within the potential widow of 0.01–3 V (vs Li/Li^+). f) Rate capability of VN nanowires and 3D VN–RGO composite electrodes at various current densities ranging from 0.1 A g^{-1} to 5 A g^{-1}.

measured currents. The pseudocapacitive contribution is ≈80% for the VN–RGO composite, which is closed to ≈82% for VN nanowire electrode (Figure S9, Supporting Information). This result suggests that VN nanowire electrode is pseudocapacitive in nature during the charge storage process. Meanwhile, VN–RGO composite still keeps the pseudocapacitive characteristics of VN nanowires with the addition of RGO. In order to further confirm the pseudocapacitive characteristic of charge storage, electrical impedance spectroscopy (EIS) measurements were conducted. The obtained Nyquist plots (Figure 4d) consist of two parts: a semicircle in the high frequency and an oblique straight line in the low frequency. Typically, the high frequency semicircle is associated with charge transfer resistance (R_{ct}).[21,25] Interestingly, VN–RGO electrode has a smaller R_{ct} (≈107 Ω) than that of VN electrode (≈138 Ω), which indicates that the addition of RGO is helpful to improve the charge transfer kinetics. In the low frequency region, the angle between the oblique line with *Z*-axis is larger than 45°, which indicates that the Li-ion intercalation in the as-prepared VN nanowires and VN–RGO composites is not limited by the diffusion process.[21] In other words, EIS measurements prove that as-prepared VN and VN–RGO electrodes are able to accommodate Li-ion though pseudocapacitive processes. The pseudocapacitive characteristic of VN and VN–RGO electrodes can still keep at the high mass loading (≈1 mg) as shown in Figures S10 andS11 (Supporting Information).

The galvanostatic charge-discharge voltage profiles over VN and VN–RGO electrodes at a current density of 0.1 A g^{-1} in the potential window 0.01–3 V (vs Li/Li^+) are displayed in Figure 4e. The charge and discharge profiles are a feature like a triangular in full work potential region, which is similar to 2D layered materials such as Mxenes[31] and graphene,[32] and but different from other negative materials with an obvious charge/discharge plateau, such as $Li_4Ti_7O_{12}$ (1.5 V vs Li/Li^+),[21] graphite (≈0.1 V vs Li/Li^+),[11] Si (0–0.2 V vs Li/Li^+),[15] Fe_3O_4 (0.8 V vs Li/Li^+),[13] and TiO_2 (1.7 V vs Li/Li^+).[33] Figure 4f shows that the discharge capacity of VN–RGO composite is ≈640 mAh g^{-1} at 0.1 A g^{-1}, which is higher than that of as-prepared VN nanowires (≈400 mAh g^{-1}). Additionally, VN–RGO composite shows a good rate performance. For example, at the high rates of 1 and 5 A g^{-1}, the specific capacity of VN–RGO composite remains ≈470 and ≈270 mAh g^{-1}, ≈73% and ≈42% of initial specific capacity, respectively. In contrast, the specific capacity of as-prepared VN nanowires is ≈243 and ≈120 mAh g^{-1}, ≈61% and ≈30% of initial specific capacity, respectively. Furthermore, VN–RGO composite electrode also exhibits excellent cycle stability as shown in Figure S12 (Supporting Information). After 2000 discharge/charge cycles at a high current density of 5 A g^{-1}, the specific capacity still keeps ≈90% of initial capacity. These results clearly demonstrate an important role of 3D architecture of the VN–RGO composite in enhanced electrochemical performance. Such extraordinary properties of 3D VN–RGO composite make it a good candidate for hybrid supercapacitor with an improved energy density and power density.

Activated carbons are widely used for positive materials in HLICs due to their high surface area, low cost, and physic or chemical stability (> 4.5 V vs Li/Li^+). Usually, the capacitive charge storage for activated carbon is strongly related to surface area and pore structure in organic electrolytes.[34,35] Therefore, the control of pore size distribution and the improvement of BET surface area are essential to improve the energy and power densities of activated carbon. In this work, activated polyaniline derived carbon (APDC) was prepared by carbonization and followed by KOH action of the polyaniline nanorod (more details about the preparation seen in our previous work in *ref* 36 and 37). The as-prepared APDC exhibits rod morphology (**Figure 5**a) and porous structure with BET surface area of 3343 m^2 g^{-1} and a narrow pore size distribution (average pore size of ≈3 nm, Figure 5b). Furthermore, APDC has a large pore volume (2.53 cm^3 g^{-1}) and high mesopore ratio (≈80%) due to the well-developed pore structure, which benefits to the diffusion and transport of electrolyte ions during the rapid charge/discharge process. As expected, APDC has an excellent electrochemical performance in organic electrolyte. Figure 5c shows the CV curves of APDC electrode over 3.0–4.5 V (vs Li/Li^+) in a Li half-cell system. The CV curves are relatively rectangular in shape and the charge/discharge curves are nearly straight lines (Figure 5d), indicating a standard capacitive behavior of EDLC. The APDC electrode had an relatively high capacity of ≈189.3 F g^{-1} (≈78.9 mAh g^{-1}) at 0.2 A g^{-1}, excellent rate capability of 124.6 F g^{-1} (≈51.9 mAh g^{-1}) at 10 A g^{-1}, and good cycle stability (≈86% after 2000 cycles) (Figure S13, Supporting Information). This capacity of APDC is higher than what has been reported for conventional activated carbons or other porous carbons in the same voltage range (≈30–60 mAh g^{-1} at 0.1–0.3 A g^{-1}).[14–16,21,33]

Before fabricating a HLIC, the following steps should be considered due to the electrochemical characteristics of VN–RGO and APDC. VN–RGO electrode was pre-activated for 10 cycles at 100 mA g^{-1} in a Li half-cell to obtain high efficiency and then lithiated to 0.5 V, and then the pre-activated VN–RGO anode was coupled with an APDC cathode to fabricate a hybrid Li-ion supercapacitor (VN–RGO//VN). The mass ratio of APDC to VN–RGO was 4 due to the charge balance between the cathode and anode.[13,15] The voltage window of 0–4 V was chosen to avoid the oxidative decomposition of electrolytes and achieve long cycle life.[15] The CV curves of VN–RGO//APDC HLIC are shown in **Figure 6**a. Different from the symmetric supercapacitor with rectangular CV shape, VN–RGO//APDC HLIC shows a slight deviation from the ideal rectangular shape due to the synergistic effect of two different energy-storage mechanisms. As the sweep rate increases, the shape of CV curves is still retained. Figure 6b shows the charge/discharging curves at different current densities. These curves exhibit approximately linear slope. The specific capacitance values of VN–RGO//APDC HLIC (based on total mass of cathodic and anodic active materials) were 73, 65, 55.6, 49.3, 42, 28.9 F g^{-1} at the current densities of 0.1, 0.2, 0.5, 0.8, 1, 2, 5 A g^{-1}, respectively (Figure 6c). Those values were more than 1.5–2 times higher than those of VN//APDC HLIC. Furthermore, VN–RGO//APDC HLIC (Figure 6d) also exhibits a good cycle stability with the capacity retention of ≈83% after 1000 cycles at a high current density of 2 A g^{-1}, while the Coulombic efficiency is at nearly 100% during the cycles.

The Ragone plot (energy density vs power density) of VN–RGO//APDC HLIC is shown in **Figure 7**. At a power density of 200 W kg^{-1}, VN–RGO//APDC HLIC can achieve a high energy density of ≈162 Wh kg^{-1}, which is higher than VN//APDC

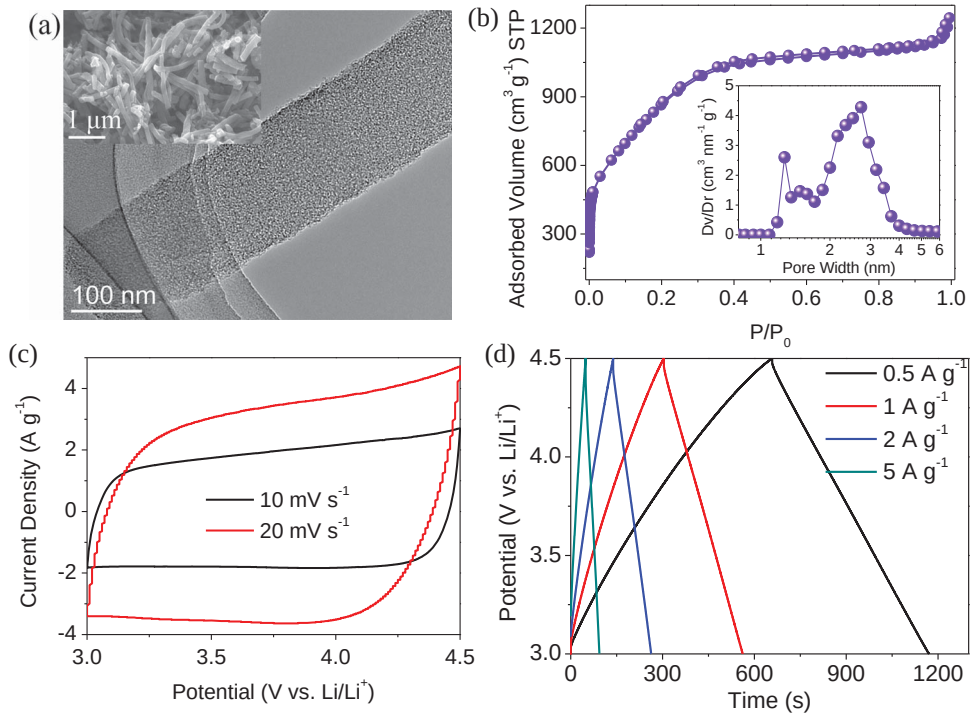

Figure 5. a) TEM image and inset SEM image showing the rod morphology of APDC porous carbon. b) Nitrogen adsorption-desorption isotherms of APDC. Inset image is the pore size distribution of APDC calculated using a NLDFT model. c) CV curves of APDC within the potential region of 3–4.5 V (vs Li/Li$^+$). d) Galvanostatic charge/discharge curves of APDC at different current densities.

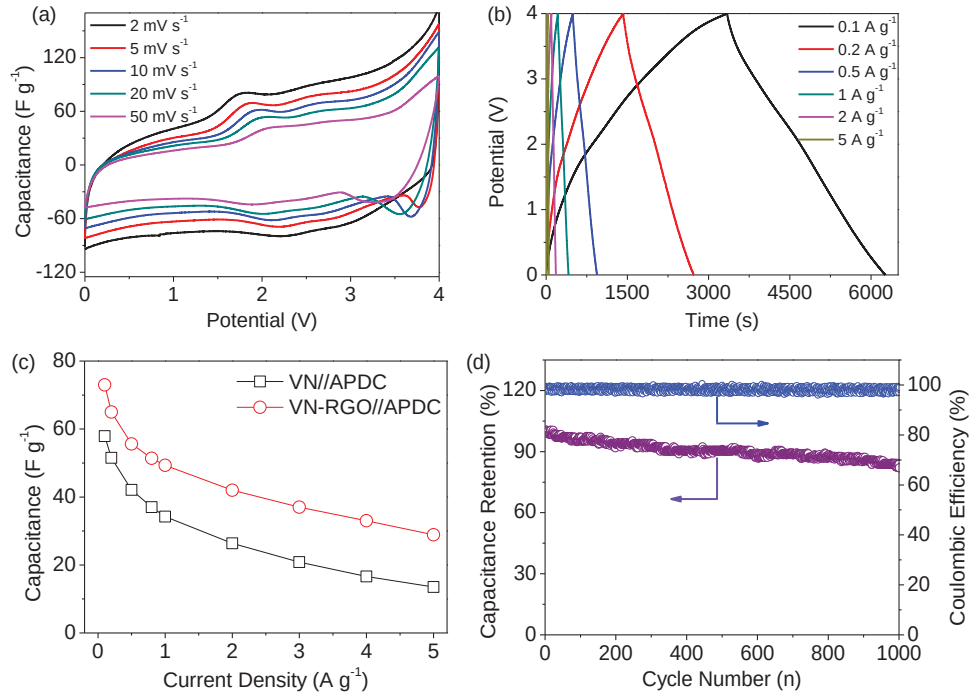

Figure 6. Electrochemical performance of 3D VN–RGO//APDC HLIC: a) CV curves at various scan rates ranging from 2 to 50 mV s^{-1}, b) galvanostatic charge/discharge curves at different current densities of 0.1–5 A g^{-1}, c) specific capacitance values calculated from galvanostatic charge/discharge curves under different current densities, d) cycle stability for 1000 cycles at a current density of 2 A g^{-1} and the corresponding columbic efficiency of ≈100%.

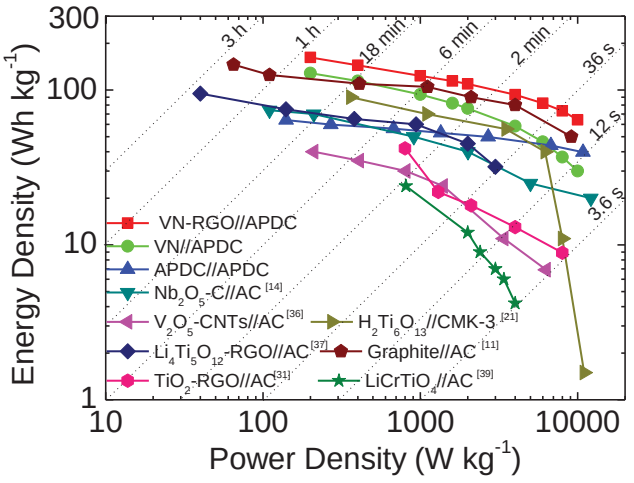

Figure 7. Ragone plots of 3D VN–RGO//APDC and VN//APDC HLICs as well as APDC//APDC symmetric supercapacitor. The energy and power densities are compared with other reported HLICs: Nb_2O_5//AC,[14] V_2O_5-CNTs//AC,[36] $Li_4Ti_5O_{12}$-rGO//AC,[37] TiO_2-RGO//AC,[31] $H_2Ti_6O_{13}$//CMK-3,[21] graphite//AC,[11] $LiCrTiO_4$//AC.[39]

HLIC (≈129 Wh kg^{-1}) (Figure S14, Supporting Information) and symmetric APDC//APDC supercapacitor (≈60 Wh kg^{-1}) (Figure S15, Supporting Information). Even at an ultra-high power density of 10 kW kg^{-1}, VN–RGO//APDC HLIC can still deliver ≈64 Wh kg^{-1}. In addition, the Ragone plot shows that the power and energy densities of VN–RGO//APDC HLIC is higher compared with similar Li-ion hybrid systems including Nb_2O_5 //AC,[14] V_2O_5-CNTs//AC,[38] $Li_4Ti_5O_{12}$//AC,[39,40] TiO_2–RGO//AC,[33] $H_2Ti_6O_{13}$//CMK-3,[21] $LiCrTiO_4$//AC,[41] graphite//AC,[11,42] $LiNi_{0.5}Mn_{1.5}O_4$//AC,[43] and TiP_2O_7//AC.[44] The superior electrochemical performance of VN–RGO//APDC hybrid device can be attributed to the following aspects: Firstly, VN nanowires electrode is majorly pseudocapacitive in nature with a wide working potential (0.01–3 V), while 3D VN–RGO composite still retains the pseudocapacitive characteristics of VN nanowires with the addition of RGO. Secondly, the 3D porous structure of VN–RGO composite with the increased BET surface area improves the accessibility of the composite to the electrolyte ions and the charge transfer kinetics; accordingly, high electrochemical utilization of VN nanowires is ensured. Lastly, the high surface area and narrow pore size distribution of APDC rods with short pore length are favorable for adsorption/desorption Li ions to form a larger amount of double layers and helps to the transport of the electrolyte ions, providing both improved energy density and good rate capability. As stated above, VN–RGO//APDC HLIC would be recognized as a promising energy-storage device.

3. Conclusions

In summary, we demonstrated that the charge storage in VN nanowires and 3D VN–RGO composite majorly arises from a pseudocapacitive process via various analytical methods. Due to the unique 3D porous structure of VN–RGO composite, it exhibits much better charge storage and rate capability compared with pure VN nanowires. Thus, a HLIC is fabricated by coupling a 3D VN–RGO anode and a porous carbon rod cathode for the first time. This hybrid device with a high working voltage window up to 4 V owing to the wide range of Li-ion intercalation/detercalation voltage (0.01–3 V vs Li/Li^+) of VN–RGO. Furthermore, VN–RGO//APDC HLIC can deliver a high energy density of ≈162 Wh kg^{-1} at 200 W kg^{-1}. Even at a high power density of 10 kW kg^{-1}, VN–RGO//APDC HLIC can still deliver ≈64 Wh kg^{-1}. The results presented here indicate that designing a 3D porous VN–RGO composite with pseudocapacitive characteristics is an effective approach to boost the energy and power densities of hybrid supercapacitors.

4. Experimental Section

Preparation of 3D Structural VN–RGO Composite: 0.2 g NH_4VO_3 was dissolved in a 50 mL solution mixture of water and ethanol with a volume ratio of 9:1. The solution pH was adjusted to 2–3 by slowly adding HCl, and then transferred to a 100 mL Teflon-lined autoclave. 30 mL GO solution (2 mg mL^{-1}) was added into the precursor solution in the autoclave. The autoclave was heated to 180 °C for 24 h, and then let it cool down to room temperature. The as-prepared sample was immersed in to distilled water for several times. After that, the obtained sample was freeze-dried overnight, followed by thermal treatment at 500 °C for 3h in Ar/NH_3 gas (40/40 sccm). For comparison, pure VN nanowires and VN–RGO with different RGO mass ratios were prepared via the same procedure.

Structural Characterization: Field emission scanning electron microscopy (FESEM, JSM 6701F, JEOL, Japan) was employed to investigate the surface morphologies of as-prepared samples. Transmission electron microscope (TEM, JEOL 2100 FEG) was employed to investigate the microstructure of as-prepared samples. Powder X-ray diffraction (XRD, Rigaku D/Max-2400, Japan) was performed using Cu-Kα radiation to investigate the structure and composition of the samples. Four probe method (MCP-T610, Mitsubishi) was used to measure the electron conductivity of the samples. Raman spectra of VN and VN–RGO were recorded using a microRaman spectroscope (JY-HR800, the excitation wavelength of 532 nm). The *C* mass ratio in VN–RGO sample were analyzed by Vario EL (Elementar, Germany). The nitrogen adsorption-desorption isotherm measurements were performed on an ASAP 2020 volumetric adsorption analyzer (Micromeritics, USA) at 77 K.

Fabrication of Half-Cell and Hybrid Device: All the supercapacitor devices studied for the material performance in this work were fabricated using the two-electrode standard method. For fabrication of VN–RGO composite electrode, 80 wt% of active material VN–RGO, 10 wt% of acetylene black as the conducting filler, and 10 wt% of polyvinylidene fluoride (PVDF) in methyl-2-pyrrolidone (NMP) were well mixed and then coated on the copper foil which served as a current collector. After heated at 110 °C for 10 h under vacuum, the sheet was pressed and punched into 10 mm diameter electrodes with a mass loading of 1–1.5 mg. For the cathode materials activated polyaniline porous carbon (APDC), 90 wt% APDC and 10 wt% polytetrafluoroethylene (PTFE) were mixed and then were rolled into thin sheets. After heated at 110 °C for 10 h, the sheet was pressed and cut into 10 mm × 10 mm electrodes. After that, the APDC cathode electrodes were dried over-night at 160 °C under vacuum and then were transferred into glove box filled with Ar. The current collector of cathode electrode is Al foil. In order to study the kinetic mechanism of VN and VN–RGO electrodes, we reduced the mass loading of active materials to 0.1–0.15 mg with the same procedure. For half cells, both anode and cathode was tested using coin type cells (2032), where Li metal foil was used to as the counter and reference electrode, and 1 M $LiPF_6$ dissolved in 1:1 v/v mixture of ethylene carbonate/diethyl carbonate (EC/DEC) was employed as the

electrolyte. Hybrid Li-ion capacitors were also assembled in coin cells with pre-activated VN–RGO anode (charged-discharged for 10 cycles and ending in a lithiated state at 0.5 V under a low current density of 0.1 A g^{-1}) and APDC cathode in the same electrolyte, and the mass ratio of cathode/anode was 4:1.

Electrochemical Measurements: All the electrochemical tests were carried out at room temperature. Cyclic voltammetry (CV), galvanostatic charge/discharge measurements and electrical impedance spectroscopy (EIS) studies were carried out using CHI660E (Shanghai, China). Cycle-life tests for half-cell and hybrid cells used a battery test system (Land CT2001A model, Wuhan Land Electronics. Ltd.). The specific capacitance of Li-ion supercapacitor was calculated using the following equation:

$$C = I / [(dE / dt) \times m] \approx I / [(\Delta E / \Delta t) \times m](Fg^{-1}) \quad (4)$$

where I is constant discharge current, Δt is the time period for a full discharge, m indicates the mass of the corresponding active electrode material, and ΔE represents the voltage change after a full discharge. The energy density (E) of Li-ion supercapacitor can be achieved by the specific capacitance (C) and the cell voltage (V) according to the following equation:

$$E = 0.5CV^2 \quad (5)$$

The power density (P) of Li-ion supercapacitor can be achieved by the energy density (E) and the discharging time (t) according to the following equation:

$$P = E / t \quad (6)$$

Supporting Information

Supporting Information is available from the Wiley Online Library or from the author.

Acknowledgements

This work was supported by the National Defense Basic Research Program of China and the National Nature Science Foundations of China (Grant No. 21203223).

Received: December 17, 2014
Revised: February 4, 2015
Published online: March 2, 2015

[1] D. Larcher, J.-M. Tarascon, *Nat. Chem.* **2015**, *7*, 19.
[2] K. Naoi, S. Ishimoto, J-I Miyamoto, W. Naoi, *Energy Environ. Sci.* **2012**, *5*, 9363.
[3] B. C. Melot, J.-M. Tarascon, *Acc. Chem. Res.* **2013**, *46*, 1226.
[4] J. Lee, A. Urban, X. Li, D. Su, G. Hautier, G. Ceder, *Science* **2014**, *343*, 519.
[5] P. Simon, Y. Gogotsi, *Nat. Mater.* **2008**, *7*, 845.
[6] V. Augustyn, P. Simon, B. Dunn, *Energy Environ. Sci.* **2014**, *7*, 1597.
[7] B. Dunn, H. Kamath, J.-M. Tarascon, *Science* **2011**, *334*, 928.
[8] Y. Gogotsi, P. Simon, *Science* **2011**, *334*, 917.
[9] V. Aravindan, J. Gnanaraj, Y.-S. Lee, S. Madhavi, *Chem. Rev.* **2014**,*114*, 11619.
[10] J. Come, M. Naguib, P. Rozier, M. W. Barsoum, Y. Gogotsi, P.-L. Taberna, M. Morcrette, P. Simon, *J. Electrochem. Soc.* **2012**, *159*, A1368.
[11] V. Khomenko, E. Raymundo-Piñero, F. Béguin, *J. Power Sources* **2008**, *177*, 643.
[12] S. R. Sivakkumar, A. G. Pandolfo, *Electrochim. Acta* **2012**, *65*, 280.
[13] F. Zhang, T. Zhang, X. Yang, L. Zhang, K. Leng, Y. Huang, Y. Chen, *Energy Environ. Sci.* **2013**, *6*, 1623.
[14] E. Lim, H. Kim, C. Jo, J. Chun, K. Ku, S. Kim, H. I. Lee, I.-S. Nam, S. Yoon, K. Kang, J. Lee, *ACS Nano* **2014**, *8*, 8968.
[15] R. Yi, S. Chen, J. Song, M. L. Gordin, A. Manivannan, D. Wang, *Adv. Funct. Mater.* **2014**, *24*, 7433.
[16] H. Wang, Z. Xu, Z. Li, K. Cui, J. Ding, A. Kohandehghan, X. Tan, B. Zahiri, B. C. Olsen, C. M. B. Holt, D. Mitlin, *Nano Lett.* **2014**, *14*, 1987.
[17] V. Augustyn, J. Come, M. A. Lowe, J. W. Kim, P. L. Taberna, S. H. Tolbert, H. D. Abruña, P. Simon, B. Dunn. *Nat. Mater.* **2013**, *12*, 518.
[18] Z. Chen, V. Augustyn, X. Jia, Q. Xiao, B. Dunn, Y. Lu, *ACS Nano* **2012**, *6*, 4319.
[19] T. Brezesinski, J. Wang, S. H. Tolbert, B. Dunn. *Nat. Mater.* **2010**, *9*, 146.
[20] P. Han, W. Ma, S. Pang, Q. Kong, J. Yao, C. Bi, G. Cui, *J. Mater. Chem. A* **2013**, *1*, 5949.
[21] Y. Wang, Z. Hong, M. Wei, Y. Xia, *Adv. Funct. Mater.* **2012**, *22*, 5185.
[22] Q. Wang, Z. Wen, J. Li, *Adv. Funct. Mater.* **2006**, *16*, 2141.
[23] T. Brezesinski, J. Wang, J. Polleux, B. Dunn, S. H. Tolbert, *J. Am. Chem. Soc.* **2009**, *131*, 1802.
[24] Q. Sun, Z.-W. Fu, *Electrochim. Acta* **2008**, *54*, 403.
[25] a) K. Zhang, H. Wang, X. He, Z. Liu, L. Wang, L. Gu, H. Xu, P. Han, S. Dong, C. Zhang, J. Yao, G. Cui, L. Chen, *J. Mater. Chem.* **2011**, *21*, 11916; b) R. Wang, X. Yan, J. Lang, Z. Zheng, P. Zhang, *J. Mater. Chem. A.* **2014**, *2*, 12724; c) Z. H. Gao, H. Zhang, G. P. Cao, M. F. Han, Y. S. Yang, *Electrochim. Acta* **2013**, *87*, 375.
[26] a) D. Choi, G. E. Blomgren, P. N. Kumta, *Adv. Mater.* **2006**, *18*, 1178; b) G. Cui, L. Gu, A. Thomas, L. Fu, P. A. V. Aken, M. Antonietti, J. Maier, *ChemPhysChem* **2010**, *11*, 3219.
[27] a) X. Lu, M. Yu, T. Zhai, G. Wang, S. Xie, T. Liu, C. Liang, Y. Tong, Y. Li, *Nano Lett.* **2013**, *13*, 2628; b) X. Lu, T. Liu, T. Zhai, G. Wang, M. Yu, S. Xie, Y. Ling, C. Liang, Y. Tong, Y. Li, *Adv. Energy Mater.* **2014**, *4*, 1300994.
[28] a) X. Xiao, X. Peng, H. Jin, T. Li, C. Zhang, B. Gao, B. Hu, K. Huo, J. Zhou, *Adv. Mater.* **2013**, *25*, 5091; b) L. Zhang, C. M. B. Holt, E. J. Luber, B. C. Olsen, H. Wang, M. Danaie, X. Cui, X. H. Tan, V. W. Lui, W. P. Kalisvaart, D. Mitlin, *J. Phys. Chem. C* **2011**, *115*, 24381.
[29] C. M. Ghimbeu, E. Raymundo-Piñero, P. Fioux, F. Béguin, C. Vix-Guterl, *J. Mater. Chem.* **2011**, *21*, 13268.
[30] J. Wang, J. Polleux, J. Lim, B. Dunn, *J. Phys. Chem. C* **2007**, *111*, 14925.
[31] a) J. Come, M. Naguib, P. Rozier, M. W. Barsoum, Y. Gogotsi, P.-L. Taberna, M. Morcrette, P. Simon, *J. Electrochem. Soc.* **2012**, *159*, A1368; b) M. Naguib, J. Halim, J. Lu, K. M. Cook, L. Hultman, Y. Gogotsi, M. W. Barsoum, *J. Am. Chem. Soc.* **2013**, *135*, 15966.
[32] Z. Weng, F. Li, D.-W. Wang, L. Wen, H.-M. Cheng, *Angew. Chem. Int . Ed.* **2013**, *52*, 3722.
[33] H. Kim, M.-Y. Cho, M.-H. Kim, K.-Y. Park, H. Gwon, Y. Lee, K. C. Roh, K. Kang, *Adv. Energy Mater.* **2013**, *3*, 1500.

[34] Y. Korenblit, A. Kajdos, W. C. West, M. C. Smart, E. J. Brandon, A. Kvit, J. Jagiello, G. Yushin, *Adv. Funct. Mater.* **2012**, *22*, 1655.
[35] Y. Zhai, Y. Dou, D. Zhao, P. F. Fulvio, R. T. Mayes, S. Dai, *Adv. Mater.* **2011**, *23*, 4828.
[36] R. T. Wang, J. W. Lang, X. B. Yan, *Sci. China Chem.* **2014**, *57*, 1570.
[37] R. T. Wang, X. B. Yan, *Sci. Rep.* **2014**, *4*, 3712.
[38] Z. Chen, V. Augustyn, J. Wen, Y. Zhang, M. Shen, B. Dunn, Y. Lu, *Adv. Mater.* **2011**, *23*, 791.
[39] K. Leng, F. Zhang, L. Zhang, T. Zhang, Y. Wu, Y. Lu, Y. Huang, Y. Chen, *Nano Res.* **2013**, *6*, 581.
[40] Y. Lei, Z.-H. Huang, Y. Yang, W. Shen, Y. Zheng, H. Sun, F. Kang, *Sci. Rep.* **2013**, *3*, 2477.
[41] V. Aravindan, W. Chuiling, S. Madhavi, *J. Mater. Chem.* **2012**, *22*, 16026.
[42] M.-S. Park, Y.-G. Lim, J.-H. Kim, Y.-J. Kim, J. Cho, J.-S. Kim, *Adv. Energy Mater.* **2011**, *1*, 1002.
[43] H. Wu, C. V. Rao, B. Rambabu, *Mater. Chem. Phys.* **2009**, *116*, 532.
[44] V. Aravindan, M. V. R. Madhavi, S. G. Mhaisalkar, G. V. Subba Rao, B. V. R. Chowdari, *J. Power Sources* **2011**, *196*, 8850.